

Article

# A Graphene-Based Microfluidic Platform for Electrocrystallization and In Situ X-ray Diffraction

Shuo Sui, Yuxi Wang, Christos Dimitrakopoulos and Sarah L. Perry \* 

Department of Chemical Engineering, University of Massachusetts Amherst, MA 01003, USA; ssui@umass.edu (S.S.); yuxiwang@engin.umass.edu (Y.W.); dimitrak@umass.edu (C.D.)

\* Correspondence: perrys@engin.umass.edu

Received: 16 December 2017; Accepted: 30 January 2018; Published: 1 February 2018

**Abstract:** Here, we describe a novel microfluidic platform for use in electrocrystallization experiments. The device incorporates ultra-thin graphene-based films as electrodes and as X-ray transparent windows to enable in situ X-ray diffraction analysis. Furthermore, large-area graphene films serve as a gas barrier, creating a stable sample environment over time. We characterize different methods for fabricating graphene electrodes, and validate the electrical capabilities of our device through the use of methyl viologen, a redox-sensitive dye. Proof-of-concept electrocrystallization experiments using an internal electric field at constant potential were performed using hen egg-white lysozyme (HEWL) as a model system. We observed faster nucleation and crystal growth, as well as a higher signal-to-noise for diffraction data obtained from crystals prepared in the presence of an applied electric field. Although this work is focused on the electrocrystallization of proteins for structural biology, we anticipate that this technology should also find utility in a broad range of both X-ray technologies and other applications of microfluidic technology.

**Keywords:** microfluidics; electrocrystallization; protein crystallization; in situ diffraction; serial crystallography

## 1. Introduction

The application of both internal and external electric fields has long been shown to modulate the rate of protein crystallogenesis, and serves as a possible tool for enhancing crystal quality [1–5]. The presence of an electric field during protein crystallization has been shown to affect both the rate of nucleation and the rate of crystal growth by controlling the local concentration and concentration gradients of proteins and the associated crystallization reagents [1–14]. These methods have the potential to improve the success rate associated with protein crystallogenesis and enhance our understanding of the structure–function relationship in challenging biomacromolecular targets.

Electrocrystallization platforms have been reported for a variety of crystallization schemes, including batch [6–11,14–20], vapor diffusion [5,13–16], and counter-diffusion [21], taking advantage of both internal [6,7,12–14,19–22] and external electric fields [5,8–10,15,18,23]. These strategies have also explored the effects of constant (DC) [5–7,13–17,20–22] and alternating (AC) electric fields [8–12,16–18]. However, the benefits observed for the various electrode arrangements and crystallization setups reported to date have been limited by the need to manually harvest crystals for subsequent diffraction analysis.

Microfluidic and microscale devices have a demonstrated potential to enable both protein crystallization and in situ X-ray diffraction. Such platforms have been increasingly harnessed to facilitate the diffraction analysis of challenging targets for both static and dynamic structure determination. Various platforms have been developed to improve the growth and subsequent mounting of tiny and fragile crystals for X-ray diffraction analysis [24–28], including dense array-style

devices [29–41], platforms for the lipidic cubic phase crystallization of membrane proteins [42,43], and thin-film sandwich devices [44]. In the meantime, the challenges of such platforms lie in the need to maintain a protected sample environment, as well as minimize the interference of device materials with the subsequent X-ray analysis. To address these two issues, we recently developed a microfluidic device architecture that takes advantage of large-area sheets of graphene [45]. The use of atomically-thin graphene films minimizes the amount of material surrounding a crystal, while serving as a vapor-diffusion barrier that is stable against significant water loss over the course of weeks. This approach enables the incubation of protein crystallization trials and direct in situ analysis of the resulting crystals. Here, we harness the intrinsic conductivity of graphene [46,47] to enable electrocrystallization experiments in the precisely controlled microfluidic geometry of our device, along with an in situ X-ray analysis of the resulting crystals.

## 2. Materials and Methods

### 2.1. Graphene Film Preparation

Large-area graphene was synthesized on a copper substrate (Graphene Platform, Tokyo, Japan) by chemical vapor deposition in a quartz tube furnace (Planar Tech, The Woodlands, TX, USA) using standard methods [48–51]. After synthesis, the back side of the copper substrate was scrubbed with a Kimwipe to remove residual graphene. Patterning of the graphene electrodes was achieved using two different methods. The first method simply used thin-tip tweezers (TDI International Inc., Tucson, AZ, USA) to scratch a narrow line into the graphene/copper film. The second method defined the desired structure of the electrodes using a protective mask made from a piece of thermal release tape (Semiconductor Equipment Corp., Moorpark, CA, USA) cut to the desired shape using a cutting plotter (Graphtech CE6000, Irvine, CA, USA), followed by a five-minute etching of the exposed graphene by an oxygen plasma (Harrick Plasma, Ithaca, NY, USA). Following the patterning of the graphene electrodes, a roughly 500-nm thick layer of poly(methylmethacrylate) (950PMMA A4, Microchem, Westborough, MA, USA) was then spin coated (Specialty Coating Systems, Amherst, NH, USA) onto the graphene at 1000 rpm to serve as a support layer. The PMMA film was cured at 120 °C for 10 min. The resulting PMMA/graphene film was then released from the copper substrate by back-etching of the copper in an aqueous solution of FeCl<sub>3</sub> copper etchant (Transene, Danvers, MA, USA) for 3 h, followed by three rinse cycles in MilliQ water (18.2 MΩ-cm, Millipore Inc., Billerica, MA, USA). The graphene film floats on the surface of water, and was transferred directly onto the target substrate by lifting it from the water surface. The assembled layers were then allowed to dry at room temperature.

### 2.2. Device Architecture

The structure of the microfluidic platform was designed to enable the application of an internal electrical field to the crystallization solution through patterned graphene electrodes (Figure 1). The overall device structure was assembled around a chamber cut into a 100-μm double-sided adhesive-backed polyester film (Adhesive Research #90668, Glen Rock, PA, USA) using a cutting plotter (Graphtec CE6000, Irvine, CA, USA). The layer containing the patterned graphene/PMMA electrode was adhered onto this film with the gap in the electrodes located near the center of the chamber. A supporting frame of cyclic olefin copolymer (COC, Topas Advanced Polymers, Florence, KY, USA) with window structures aligned to the crystallization chamber was adhered to the outside of the notched graphene/PMMA film to provide mechanical stability. After filling of the device, the chamber was sealed with a top layer containing a smaller, unmodified graphene/PMMA film, supported on a COC frame. In contrast to the electrode layer, the top graphene/PMMA film was oriented with the PMMA layer facing the crystallization chamber so that the graphene would not contribute to the conductivity of the cell. Finally, the small side features cut into the polyester film and the top support layer of COC were filled by a gallium–indium liquid alloy (Sigma Aldrich, St. Louis, MO, USA) to create the electrode contact between graphene films and the electrode needles running to

a power supply (Figure 2). It should be noted that the thickness of the adhesive layer used to define the crystallization chamber can be modulated to match the size of the resulting crystals, and minimize the amount of excess liquid surrounding the crystals during data collection.

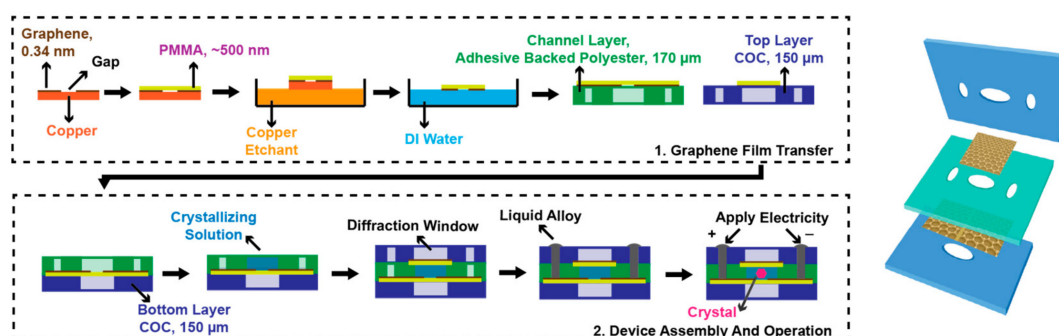


**Figure 1.** Schematic illustration of the fabrication scheme and device architecture for thin-film graphene-based microfluidics. (1) A patterned graphene film on copper is first coated with a layer of poly(methylmethacrylate) (PMMA), and then released from the copper substrate by etching. The subsequent film is floated on the surface of water for transfer to either an adhesive-backed polyester film that defines the crystallization chamber, or a cyclic olefin copolymer film to form the top layer of the device. (2) Assembly of the device proceeded with the application of a COC bottom layer to the crystallization layer assembly to provide additional stability. Following the addition of the crystallization solution, the device is then sealed with the COC top layer. Electrical contact to the graphene electrodes is made using a liquid alloy, and the electrocrystallization experiment can take place.

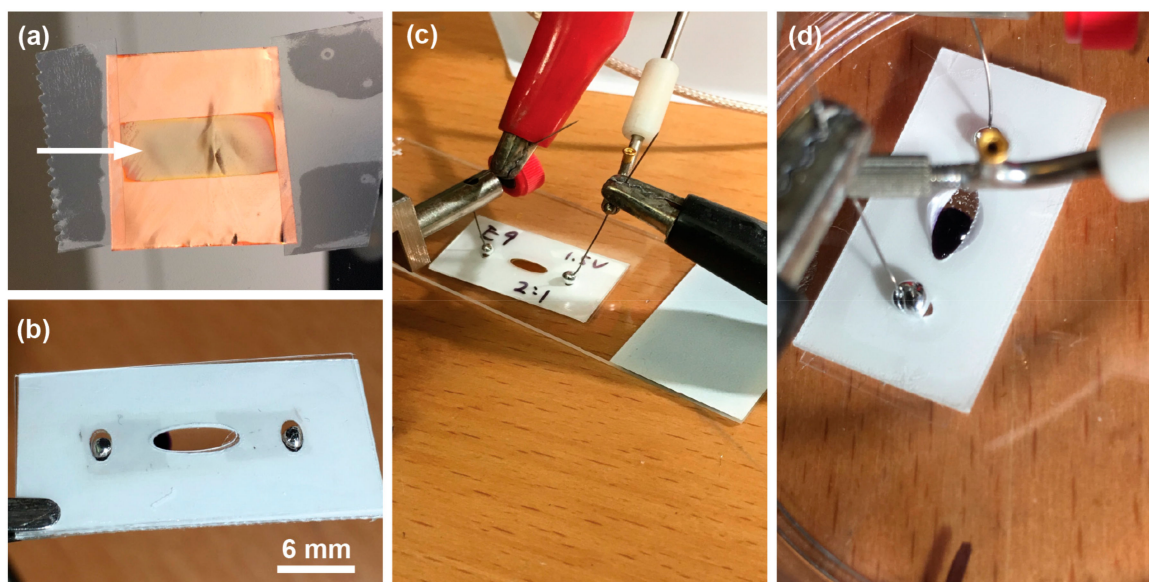


**Figure 2.** (a) Graphene film on copper growth substrate after oxygen plasma treating. The brassy yellow area in the middle of the film was exposed to the plasma, while the upper and lower regions were covered and protected by a mask created from thermal release tape. (b) A view of the patterned electrodes (regions of light grey) in an assembled device. (c) System setup for electrocrystallization experiments. Alligator clips attached to metal needles and gallium–indium alloy droplets were used to make electrical contact with the integrated graphene electrodes. (d) The presence of an applied electric field can be observed visually based on the color change of methyl viologen from clear to purple as it undergoes reduction at the cathode.

### 2.3. Electrode Characterization

To quantitatively characterize the film electrical resistance at different conditions, we measured the voltage resulting from a current sweep from 0 to 100  $\mu\text{A}$  using a semiconductor characterization system (Keithley 4200 SCS, Tektronix Inc., Beaverton, OR, USA) on intact graphene films and patterned graphene electrodes in air, and in the presence of a crystallization solution (Figure 3). We compared electrodes patterned by both physical abrasion and plasma etching. The corresponding electrical resistances were calculated based on the resultant voltage–current relationships and the device architecture. All of the tests were performed in triplicate.

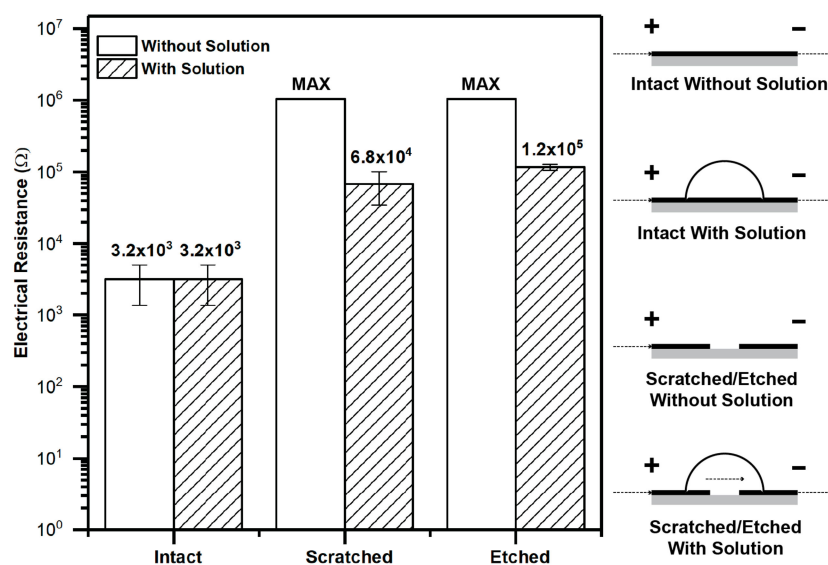


**Figure 3.** Plot of the measured average electrical resistance of an intact graphene film, a graphene film where electrodes were fabricated by physical scratching, and a graphene film where the electrode structure was created by plasma etching. Data are shown for both the electrode structure alone (without solution, clear bars) and for a device filled with crystallization solution (hatched bars), and are the average of measurements from three separate devices. The maximum resistance measured for the two electrode structures in air suggests an infinite resistance, beyond the range of the instrument.

### 2.4. Redox Chemistry Testing

Methyl viologen (MV) is a redox and oxygen-sensitive dye. A solution of methyl viologen (Sigma Aldrich, St. Louis, MO, USA) in water was prepared at 150 mM. In the presence of oxygen, methyl viologen is present as fully oxidized  $\text{MV}^{2+}$ , resulting in a colorless solution. The partially oxidized  $\text{MV}^+$  species is a brilliant purple, while the fully reduced, neutral  $\text{MV}^0$  is typically light yellow [52–54]. To test the ability of our graphene-based devices to conduct electricity and drive redox chemistry, 10  $\mu\text{L}$  of fully oxidized methyl viologen was placed onto a patterned graphene electrode. An applied voltage was then slowly increased from 0 V to 3 V, and then held at 3 V for 5 min, during which time the subsequent color changes were observed (Figure 4).

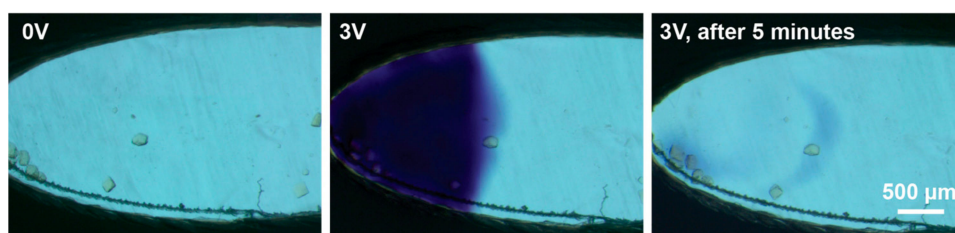


**Figure 4.** Optical micrographs of an electrocrystallization device containing 150 mM of methyl viologen (MV) and crystals of lysozyme under the influence of 0 V, 3 V, and 3 V at longer times. The initial color change from clear to purple is the result of the reduction of  $MV^{2+}$  to  $MV^+$ , while the subsequent loss of color at higher voltages and longer times is due to the further reduction from  $MV^+$  to  $MV^0$ . The pale yellow color of the  $MV^0$  was difficult to discern compared to the fully oxidized  $MV^{2+}$  species, because of the small path length in our microfluidic devices. Color changes were only observed in the vicinity of the cathode.

### 2.5. Protein Crystallization and X-ray Diffraction

Hen egg white lysozyme (HEWL, Hampton Research Inc., Aliso Viejo, CA, USA) was prepared in 50 mM of sodium acetate (Fisher) and 20% (*w/v*) glycerol (Fisher Scientific, Hampton, NH, USA) with a concentration of 80 mg/mL at pH 4.8. The protein solution was then fully mixed by vortexing with a precipitant solution containing 0.68 M of sodium chloride (Sigma, St. Louis, MO, USA) and 50 mM of sodium acetate at pH 4.8 at a volumetric ratio of 2:3. All of the solutions were filtered before use through a 0.2- $\mu$ m membrane (Millipore, Billerica, MA, USA) to remove impurities. Crystallization was performed using a microbatch-type method [55]; 3.2  $\mu$ L of mixed solution was pipetted immediately after preparation, and sealed into the device. It should be noted that the volume of solution added to the device should be carefully controlled to match the volume of the chamber, as excess liquid will be squeezed out of the chamber, and will adversely affect device sealing.

The crystallization experiment was performed in a 4 °C cold room under different applied voltages using a potentiostat (Arksen 305-2D, City of Industry, CA, USA). For a given experiment, simultaneous tests were performed on multiple devices at the applied voltage, alongside a control device with no applied voltage. Crystal growth was monitored hourly using a stereomicroscope (Zeiss SterEO Discovery V12, Oberkochen, Germany) under cross-polarized light (Figure 5a and Figure S1). After crystallization was complete, the devices were disconnected from the voltage supply, sealed in Petri dishes (Fisher Scientific, Hampton, NH, USA), and stored at 4 °C prior to X-ray analysis. Replicate crystallization experiments were performed over a range of applied voltages (0 V to 1.8 V), demonstrating the reproducibility of our approach.

The quantification of crystal size as a function of time was done using the size measurement function in ImageJ software (NIH, Bethesda, MD, USA) [56] by manually outlining crystal edges. Crystals appeared to be randomly oriented. However, the overall aspect ratio of the crystals was similar, allowing for the reasonable use of a calculated two-dimensional area to represent the three-dimensional size of a crystal. For each time point, all of the crystals in each chip were measured, and the average projected area was calculated (Figure 5b,c and Figure S2). Error bars represented the standard deviation from the mean. A comparison between crystal sizes at different time points and voltage conditions was performed using ANOVA. While the data in Figure 5 represent the results of only three individual devices, replicate experiments show similar trends, relative to controls (see Figures S1 and S2).

Immediately after crystallization, the chips were stored in 4 °C, and analyzed within a couple of days. The chip was mounted on the goniometer using a custom magnetic mounting base (Crystal Positioning Systems, Jamestown, NY, USA). The X-ray system (Rigaku XtalAB PRO MM007, Tokyo, Japan) operated at an X-ray wavelength of 1.542 Å and a beam size of ~200  $\mu$ m, along with a PILATUS3 R 200K detector (Dectris AG, Baden-Dättwil, Switzerland). The chip was initially mounted perpendicular to the beam path. Crystal targeting and focusing and were done by adjusting the

goniometer positions. The sample-to-detector distance was set at 40 mm, giving a maximum resolution of 1.95 Å. A 10-s exposure and 1° oscillation were used. Before collecting a complete dataset, the sample orientations corresponding to the first and last frames were tested to avoid overlapping signals from nearby crystals. The collected diffraction patterns were then analyzed using the HKL 3000 software package (HKL Research Inc., Charlottesville, VA, USA) for indexing, refinement, integration, and scaling. The X-ray diffraction data extended to the maximum resolution limit of the X-ray setup, showing a signal-to-noise level in the highest resolution shell of  $I/\sigma(I) > 3.0$  for all of the samples (Figure 6, Table 1).

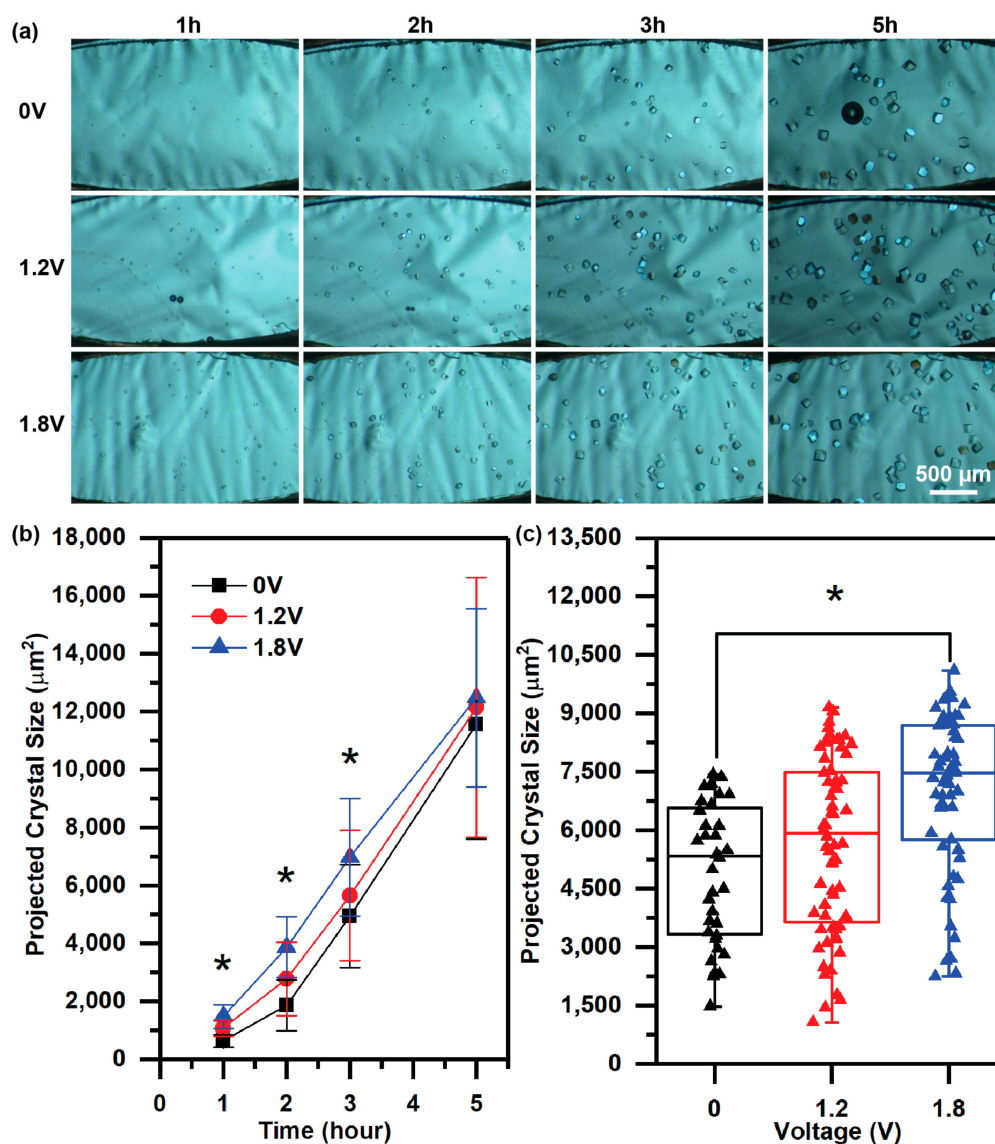


**Figure 5.** (a) Optical micrographs under cross-polarized light showing the time evolution of hen egg-white lysozyme (HEWL) crystal nucleation and growth with the application of 0 V, 1.2 V, and 1.8 V in a microfluidic device. (b) A plot of the average crystal size as a function of time from the images in (a). Error bars represent the standard deviation. (c) A box and whiskers plot of the crystal size distribution at 3 h with the application of voltages at 0 V, 1.2 V, and 1.8 V. The middle line shows the median, and the ends of the box indicate the upper and lower quartiles. \* Crystals prepared at 1.8 V at 1 h, 2 h, and 3 h were statistically larger than those prepared at 0 V, ANOVA  $p < 0.01$ .

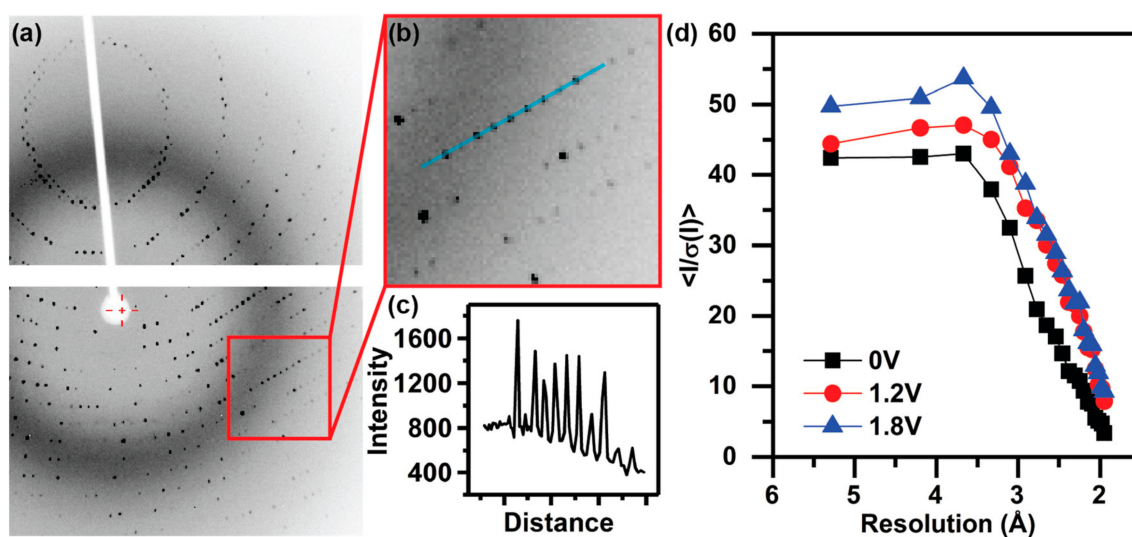


**Figure 6.** (a) A typical obtained X-ray diffraction pattern and (b) a magnified view showing details of diffracted spots. (c) Pixel intensity along the blue line in the inset indicated the high levels of signal-to-noise observed in the data. (d) A plot of signal-to-noise ratios at different resolution shells of diffraction patterns from crystals grown under different voltages.

**Table 1.** Crystallographic statistics for data obtained using graphene-based microfluidics under different applied voltages.

Parameter	0 V	1.2 V	1.8 V
<b>Data Collection</b>			
Total # Frames	50	55	90
Resolution (Å)	50–1.95 (1.98–1.95)	50–1.95 (1.98–1.95)	50–1.95 (1.98–1.95)
Space Group	P4 <sub>3</sub> 2 <sub>1</sub> 2	P4 <sub>3</sub> 2 <sub>1</sub> 2	P4 <sub>3</sub> 2 <sub>1</sub> 2
Unit Cell (Å)	a = b = 79.35, c = 37.99	a = b = 79.23, c = 38.09	a = b = 78.92, c = 38.19
<b>Single Reflections</b>			
Total Obs.	31,372	34,440	55,551
Unique Obs.	7086	8817	9053
Redundancy	4.4 (3.4)	3.9 (3.2)	6.1 (5.1)
$R_{meas}^a$	0.069 (0.399)	0.052 (0.202)	0.076 (0.255)
$R_{pim}^b$	0.031 (0.206)	0.025 (0.105)	0.031 (0.112)
$CC_{1/2}^c$	0.971 (0.883)	0.990 (0.961)	0.951 (0.890)
$\langle I/\sigma(I) \rangle$	22.69 (3.39)	33.24 (7.89)	36.98 (9.21)
Completeness (%)	76.0 (82.4)	94.6 (95.4)	97.5 (97.1)

Data in the parenthesis are from the highest resolution shell. <sup>a</sup>  $R_{meas} = \frac{\sum_{hkl} \sqrt{\frac{1}{n-1}} \sum_{j=1}^n |I_{hkl,j} - \langle I_{hkl} \rangle|}{\sum_{hkl} \sum_j I_{hkl,j}}$ , <sup>b</sup>  $R_{pim} = \frac{\sum_{hkl} \sqrt{\frac{1}{n-1}} \sum_{j=1}^n |I_{hkl,j} - \langle I_{hkl} \rangle|}{\sum_{hkl} \sum_j I_{hkl,j}}$ , where  $I$  is the reflection intensity and  $\langle I \rangle$  is its average, and  $\sqrt{\frac{n}{n-1}}$  and  $\sqrt{\frac{1}{n-1}}$  are factors for multiplicity. <sup>c</sup>  $CC_{1/2}$  is the Pearson correlation coefficient with the dataset randomly being split in half, and  $CC = \frac{\sum (x - \langle x \rangle)(y - \langle y \rangle)}{\sqrt{\sum (x - \langle x \rangle)^2 \sum (y - \langle y \rangle)^2}}$ , where  $x, y$  are single samples.

### 3. Results and Discussion

The goal of this work was to take advantage of atomically-thin, conductive graphene films to enable electrocrystallization experiments in a microfluidic device, followed by in situ X-ray diffraction analysis of the resulting crystals. This work builds on our previously reported graphene-based platform for serial crystallography [45], but requires the fabrication and integration of patterned graphene electrodes, rather than simple graphene windows.

While it is possible to create a set of electrodes by simply adhering two separate pieces of graphene to a substrate, we took advantage of a more controlled fabrication strategy to enable careful control of the electrode spacing and geometry. Here, we used a protective film of thermal release tape to facilitate direct patterning of the graphene, using an oxygen plasma. Following plasma treatment and removal of the protective film, we observed clear patterning of the graphene to reveal the underlying copper substrate (Figure 2a). Thus, the width of the resulting gap can be easily controlled to modulate the electric field strength. Experiments were typically done using a gap size of 3 mm. A roughly 500 nm-thick layer of PMMA was then spin coated onto the graphene/copper surface to facilitate the retention of electrode geometry after removal from the underlying copper substrate and transfer to the target device layers. The graphene electrodes could be observed on the fully assembled devices as areas of light grey color located on the ends of the microfluidic channel, relative to the white background of the middle adhesive channel layer of the device (Figure 2b). This design takes advantage of relatively cheap materials and fabrication strategies, such that the material cost of a single device should be on the order of \$1 (USD) or less, depending on economies of scale.

We compared the resulting electrical properties of these plasma-etched graphene electrodes with an analogous electrode layout fabricated by simple physical abrasion (Figure 3). The electrical resistance of an intact graphene film was relatively low, and highly reproducible, as expected for an atomically-thin conductive material. While the effectively infinite resistance measured for the two electrode setups in air clearly demonstrated the separation of the two electrodes, clear differences were observed in the operation of the devices in the presence of crystallization solution. Devices with the electrodes fabricated via physical abrasion showed substantially lower and more variable resistivity values compared with the plasma etching method. The lower resistance observed for the physical abrasion method suggests the presence of graphene residue in the gap area between the electrodes. Thus, while this kind of simplified fabrication scheme can be applied, it has the potential to adversely affect both the performance and reproducibility of the resulting device in electrocrystallization experiments. Subsequent experiments were performed using plasma-etched electrodes.

To further visualize the effectiveness of our devices, we utilized methyl viologen (MV) as a redox-sensitive colorimetric indicator. The solution was observed to change from colorless ( $MV^{2+}$ ) to brilliant purple ( $MV^+$ ) near the cathode upon the application of 1 V, consistent with the reported value of the redox potential for the  $MV^{2+} + e^- \rightarrow MV^+$  reaction of  $\sim 0.7$  V (Figure 2) [52–54]. A similar color change was observed for a slurry of lysozyme crystals containing methyl viologen (Figure 4). In both experiments, the observed change in color only occurred in the area of the device defined by the cathode. We hypothesize that the localization of this color change near the cathode is due to an enhancement of the redox reaction by the solid graphene electrode. Increasing the applied voltage to 3 V resulted in an intensification of the observed purple color, due to the increased generation of the  $MV^+$  species. However, after several minutes, the solution transitioned from purple to clear, as  $MV^+$  was further reduced to  $MV^0$  (Figure 4). Again, this result was expected, based on the reported redox potential for the  $MV^+ + e^- \rightarrow MV^0$  reaction [52–54]. The pale yellow color of the  $MV^0$  was difficult to discern compared to the fully oxidized  $MV^{2+}$  species, because of the small path length in our microfluidic devices. It is also noteworthy that despite the potential for water electrolysis at these applied voltages, the reaction rate on graphene electrodes is relatively slow. Thus, the formation of bubbles was typically not observed during the course of an experiment.

Having demonstrated the electrical performance of our device, we then proceeded to study the electrocrystallization of lysozyme as a function of time. With a 3-mm patterned gap on the graphene film, the applied voltage resulted in an electric field strength in the range of 0.4 V/mm to 0.6 V/mm, which is similar to a range reported in the literature [4]. As shown in Figure 5, Figures S1 and S2, the presence of an applied voltage resulted in an increased rate of protein nucleation and growth, which is consistent with previous literature reports [1–14]. Interestingly, these trends were only significant at short times. For instance, after 1 h, 2 h, and 3 h, the average size of crystals grown under the influence

of an applied voltage was statistically different compared to a control sample (Figure 5b,c), while this difference is lost by 5 h.

In addition to the effects on nucleation and growth, we did not observe a significant preferential localization of crystals within the device. This is in contrast to previous reports for the electrocrystallization of lysozyme, where crystals were typically localized near the cathode. We hypothesize that the broad spatial distribution of crystals, as well as the similar crystal size at long times, is a consequence of the relatively short time period over which these experiments were performed. The increased rate of crystal nucleation and growth associated with electrocrystallization is typically associated with the electromigration of the protein, and subsequent increases in concentration near the relevant electrode. Thus, it is possible that the crystallization conditions used here fall very close to the nucleation region such that only minimal increases in the local protein concentration were necessary to facilitate nucleation, while allowing for the appearance of crystal growth throughout the device and the similarity of crystal size at long times.

After crystallization, the devices were stored at 4 °C for several days prior to X-ray diffraction analysis. We collected a room temperature dataset from a representative crystal grown under each of the applied voltage conditions (0 V, 1.2 V, 1.8 V). Data were collected and analyzed to the maximum resolution of our diffraction setup. At this limit of 1.95 Å, the  $I/\sigma(I)$ , or signal-to-noise level in the highest resolution shell, was above 3.0 for all of the samples, and was significantly higher for those samples prepared in the presence of an electric field, than those without (Figure 6, Table 1). This high signal-to-noise was expected, due to the minimal contributions of the device materials to the level of background noise [45]. The size of the X-ray beam and the presence of nearby crystals limited the number of frames that could be collected from a given sample. While it was possible to collect nearly complete datasets for the 1.2 V and 1.8 V samples, a lower completeness was obtained for the 0 V sample. Despite these differences, the data suggest that the crystals grown in the presence of an electric field may diffract to higher resolution than crystals grown without. Unfortunately, we were unable to confirm this result directly because of the limitations of our X-ray diffraction setup. It should be noted that, although the crystal size varied between the various voltage conditions early on, this difference was lost over longer time periods. Care was taken to select crystals of similar size. Thus, the difference in the observed signal-to-noise should not be a consequence of differences in crystal size. These results agree with previous literature reports where a higher signal-to-noise [7] was observed for crystals grown in an electric field. It is important to note that this is the first report where direct, in situ measurements of the X-ray diffraction quality could be obtained on protein crystals grown via electrocrystallization, without the need for handling of fragile capillaries [16] or the use of hard X-rays to limit absorption from the crystallization cell [14].

#### 4. Summary

In conclusion, we have presented a straightforward method for the incorporation of graphene-based electrodes into an ultra-thin, X-ray compatible microfluidic platform. We have demonstrated the utility of this setup to enable in situ X-ray diffraction data collection for electrocrystallization experiments. Our data agree with previous reports, showing faster crystal nucleation and an improvement in signal-to-noise for crystals grown in the presence of an electric field. Building on these results, our microfluidic approach has the potential to enable high-throughput analysis of a tremendous range of crystallization and electric field conditions to better map out the effect of these parameters on crystal quality in general. This approach is also amenable to serial crystallography experiments, where our microfluidic array chip could be used to grow hundreds or thousands of microcrystals for serial diffraction analysis. Looking beyond structural biology, the integration of ultra-thin graphene electrodes into microfluidic devices could similarly enable powerful high-throughput experiments in a range of other fields.

**Supplementary Materials:** The following are available online at [www.mdpi.com/2073-4352/8/2/76/s1](http://www.mdpi.com/2073-4352/8/2/76/s1). Additional electrocrystallization results are available in Figures S1 and S2.

**Acknowledgments:** We acknowledge support from the NSF Science and Technology Center on Biology with X-ray Lasers (NSF-1231306). X-ray diffraction data were obtained at the University of Massachusetts Amherst Institute for Applied Life Sciences Biophysical Characterization Facility. We would like to acknowledge Lizz Bartlett and Derrick Deming for assistance with X-ray diffraction experiments, Jungwoo Lee and Jun-Goo Kwak for help with and the use of the cutting plotter, Whitney Blocher, Ryan Carpenter and Xiangxi “Zoey” Meng for help with statistical analysis, and Scott Garman and Yiliang Zhou for valuable discussions.

**Author Contributions:** Shuo Sui, Yuxi Wang and Sarah L. Perry designed and performed the experiments. Shuo Sui and Sarah L. Perry analyzed the data. All authors helped with writing the manuscript.

**Conflicts of Interest:** The authors declare no conflict of interest.

## References

1. Al-Haq, M.I.; Lebrasseur, E.; Tsuchiya, H.; Torii, T. Protein crystallization under an electric field. *Crystallogr. Rev.* **2007**, *13*, 29–64. [[CrossRef](#)]
2. Mirkin, N.; Moreno, A. Advances in crystal growth techniques of biological macromolecules. *J. Mex. Chem. Soc.* **2005**, *49*, 39–52.
3. Frontana-Uribe, B.A.; Moreno, A. On electrochemically assisted protein crystallization and related methods. *Cryst. Growth Des.* **2008**, *8*, 4194–4199. [[CrossRef](#)]
4. Hammadi, Z.; Veessler, S. New approaches on crystallization under electric fields. *Prog. Biophys. Mol. Biol.* **2010**, *101*, 38–44. [[CrossRef](#)] [[PubMed](#)]
5. Taleb, M.; Didierjean, C.; Jelsch, C.; Mangeot, J.P.; Capelle, B.; Aubry, A. Crystallization of proteins under an external electric field. *J. Cryst. Growth* **1999**, *200*, 575–582. [[CrossRef](#)]
6. Pérez, Y.; Eid, D.; Acosta, F.; Marín-García, L.; Jakoncic, J.; Stojanoff, V.; Frontana-Uribe, B.A.; Moreno, A. Electrochemically assisted protein crystallization of commercial cytochrome *c* without previous purification. *Cryst. Growth Des.* **2008**, *8*, 2493–2496. [[CrossRef](#)]
7. Gil-Alvaradejo, G.; Ruiz-Arellano, R.R.; Owen, C.; Rodríguez-Romero, A.; Rudiño-Piñera, E.; Antwi, M.K.; Stojanoff, V.; Moreno, A. Novel protein crystal growth electrochemical cell for applications in X-ray diffraction and atomic force microscopy. *Cryst. Growth Des.* **2011**, *11*, 3917–3922. [[CrossRef](#)]
8. Koizumi, H.; Fujiwara, K.; Uda, S. Role of the electric double layer in controlling the nucleation rate for tetragonal hen egg white lysozyme crystals by application of an external electric field. *Cryst. Growth Des.* **2010**, *10*, 2591–2595. [[CrossRef](#)]
9. Koizumi, H.; Uda, S.; Fujiwara, K.; Nozawa, J. Control of effect on the nucleation rate for hen egg white lysozyme crystals under application of an external ac electric field. *Langmuir* **2011**, *27*, 8333–8338. [[CrossRef](#)] [[PubMed](#)]
10. Pan, W.; Xu, H.; Zhang, R.; Xu, J.; Tsukamoto, K.; Han, J.; Li, A. The influence of low frequency of external electric field on nucleation enhancement of hen egg-white lysozyme (HEWL). *J. Cryst. Growth* **2015**, *428*, 35–39. [[CrossRef](#)]
11. Li, F.; Lakerveld, R. Influence of alternating electric fields on protein crystallization in microfluidic devices with patterned electrodes in a parallel-plate configuration. *Cryst. Growth Des.* **2017**, *17*, 3062–3070. [[CrossRef](#)]
12. Hou, D.; Chang, H.-C. AC field enhanced protein crystallization. *Appl. Phys. Lett.* **2008**, *92*, 223902. [[CrossRef](#)]
13. Flores-Hernandez, E.; Stojanoff, V.; Arreguin-Espinosa, R.; Moreno, A.; Sanchez-Puig, N. An electrically assisted device for protein crystallization in a vapor diffusion setup. *J. Appl. Cryst.* **2013**, *46*, 832–834. [[CrossRef](#)] [[PubMed](#)]
14. Martínez-Caballero, S.; Cuéllar-Cruz, M.; Demitri, N.; Polentarutti, M.; Rodríguez-Romero, A.; Moreno, A. Glucose isomerase polymorphs obtained using an ad hoc protein crystallization temperature device and a growth cell applying an electric field. *Cryst. Growth Des.* **2016**, *16*, 1679–1686. [[CrossRef](#)]
15. Taleb, M.; Didierjean, C.; Jelsch, C.; Mangeot, J.P.; Aubry, A. Equilibrium kinetics of lysozyme crystallization under an external electric field. *J. Cryst. Growth* **2001**, *232*, 250–255. [[CrossRef](#)]
16. Pareja-Rivera, C.; Cuéllar-Cruz, M.; Esturau-Escofet, N.; Demitri, N.; Polentarutti, M.; Stojanoff, V.; Moreno, A. Recent advances in the understanding of the influence of electric and magnetic fields on protein crystal growth. *Cryst. Growth Des.* **2017**, *17*, 135–145. [[CrossRef](#)]
17. Al-Haq, M.I.; Lebrasseur, E.; Choi, W.-K.; Tsuchiya, H.; Torii, T.; Yamazaki, H.; Shinohara, E. An apparatus for electric-field-induced protein crystallization. *J. Appl. Cryst.* **2007**, *40*, 199–201. [[CrossRef](#)]

18. Koizumi, H.; Uda, S.; Fujiwara, K.; Tachibana, M.; Kojima, K.; Nozawa, J. Crystallization of high-quality protein crystals using an external electric field. *J. Appl. Cryst.* **2015**, *48*, 1507–1513. [[CrossRef](#)]
19. Espinoza-Montero, P.J.; Moreno-Narváez, M.E.; Frontana-Uribe, B.A.; Stojanoff, V.; Moreno, A. Investigations on the use of graphite electrodes using a hull-type growth cell for electrochemically assisted protein crystallization. *Cryst. Growth Des.* **2013**, *13*, 590–598. [[CrossRef](#)] [[PubMed](#)]
20. Sazaki, G.; Moreno, A.; Nakajima, K. Novel coupling effects of the magnetic and electric fields on protein crystallization. *J. Cryst. Growth* **2004**, *262*, 499–502. [[CrossRef](#)]
21. Mirkin, N.; Frontana-Uribe, B.A.; Rodriguez-Romero, A.; Hernandez-Santoyo, A.; Moreno, A. The influence of an internal electric field upon protein crystallization using the gel-acupuncture method. *Acta Crystallogr. Sect. D Biol. Crystallogr.* **2003**, *59*, 1533–1538. [[CrossRef](#)]
22. Nieto-Mendoza, E.; Frontana-Uribe, B.A.; Sazaki, G.; Moreno, A. Investigations on electromigration phenomena for protein crystallization using crystal growth cells with multiple electrodes: Effect of the potential control. *J. Cryst. Growth* **2005**, *275*, e1437–e1446. [[CrossRef](#)]
23. Nanev, C.N.; Penkova, A. Nucleation of lysozyme crystals under external electric and ultrasonic fields. *J. Cryst. Growth* **2001**, *232*, 285–293. [[CrossRef](#)]
24. Sui, S.; Perry, S.L. Microfluidics: From crystallization to serial time-resolved crystallography. *Struct. Dyn.* **2017**, *4*, 032202. [[CrossRef](#)]
25. Ghazal, A.; Lafleur, J.P.; Mortensen, K.; Kutter, J.P.; Arleth, L.; Jensen, G.V. Recent advances in X-ray compatible microfluidics for applications in soft materials and life sciences. *Lab Chip* **2016**, *16*, 4263–4295. [[CrossRef](#)] [[PubMed](#)]
26. Sauter, C.; Dhouib, K.; Lorber, B. from macrofluidics to microfluidics for the crystallization of biological macromolecules. *Cryst. Growth Des.* **2007**, *7*, 2247–2250. [[CrossRef](#)]
27. Chavas, L.M.G.; Gumprecht, L.; Chapman, H.N. Possibilities for serial femtosecond crystallography sample delivery at future light sources. *Struct. Dyn.* **2015**, *2*, 041709. [[CrossRef](#)] [[PubMed](#)]
28. Weierstall, U. Liquid sample delivery techniques for serial femtosecond crystallography. *Philos. Trans. R. Soc. B* **2014**, *369*, 20130337. [[CrossRef](#)] [[PubMed](#)]
29. Guha, S.; Perry, S.L.; Pawate, A.S.; Kenis, P.J.A. Fabrication of X-ray compatible microfluidic platforms for protein crystallization. *Sens. Actuators B* **2012**, *174*, 1–9. [[CrossRef](#)] [[PubMed](#)]
30. Perry, S.L.; Guha, S.; Pawate, A.S.; Bhaskarla, A.; Agarwal, V.; Nair, S.K.; Kenis, P.J.A. A microfluidic approach for protein structure determination at room temperature via on-chip anomalous diffraction. *Lab Chip* **2013**, *13*, 3183–3187. [[CrossRef](#)] [[PubMed](#)]
31. Heymann, M.; Ophthalge, A.; Wierman, J.L.; Akella, S.; Szebenyi, D.M.; Gruner, S.M.; Fraden, S. Room-Temperature serial crystallography using a kinetically optimized microfluidic device for protein crystallization and on-chip X-ray diffraction. *IUCr* **2014**, *1*, 349–360. [[CrossRef](#)] [[PubMed](#)]
32. Kisselman, G.; Qiu, W.; Romanov, V.; Thompson, C.M.; Lam, R.; Battaile, K.P.; Pai, E.F.; Chirgadze, N.Y. X-CHIP: An integrated platform for high-throughput protein crystallization and on-the-chip X-ray diffraction data collection. *Acta Crystallogr. Sect. D Biol. Crystallogr.* **2011**, *67*, 533–539. [[CrossRef](#)] [[PubMed](#)]
33. Chirgadze, N.Y.; Kisselman, G.; Qiu, W.; Romanov, V.; Thompson, C.M.; Lam, R.; Battaile, K.P.; Pai, E.F. X-CHIP: An integrated platform for high-throughput protein crystallography. In *Recent Advances in Crystallography*; Benedict, J.B., Ed.; InTech: Vienna, Austria, 2012; pp. 87–96.
34. Hunter, M.S.; Segelke, B.; Messerschmidt, M.; Williams, G.J.; Zatsepin, N.A.; Barty, A.; Benner, W.H.; Carlson, D.B.; Coleman, M.; Graf, A.; et al. Fixed-Target protein serial microcrystallography with an X-ray free electron laser. *Sci. Rep.* **2014**, *4*, 6026. [[CrossRef](#)] [[PubMed](#)]
35. Feld, G.K.; Heymann, M.; Benner, W.H.; Pardini, T.; Tsai, C.-J.; Boutet, S.; Coleman, M.A.; Hunter, M.S.; Li, X.; Messerschmidt, M.; et al. Low-Z polymer sample supports for fixed-target serial femtosecond X-ray crystallography. *J. Appl. Cryst.* **2015**, *48*, 1072–1079. [[CrossRef](#)]
36. Baxter, E.L.; Aguila, L.; Alonso-Mori, R.; Barnes, C.O.; Bonagura, C.A.; Brehmer, W.; Brunger, A.T.; Calero, G.; Caradoc-Davies, T.T.; Chatterjee, R.; et al. High-Density grids for efficient data collection from multiple crystals. *Acta Crystallogr. Sect. D Biol. Crystallogr.* **2016**, *72*, 2–11. [[CrossRef](#)] [[PubMed](#)]
37. Lyubimov, A.Y.; Murray, T.D.; Koehl, A.; Araci, I.E.; Uervirojnangkoon, M.; Zeldin, O.B.; Cohen, A.E.; Soltis, S.M.; Baxter, E.L.; Brewster, A.S.; et al. Capture and X-ray diffraction studies of protein microcrystals in a microfluidic trap array. *Acta Crystallogr. Sect. D Biol. Crystallogr.* **2015**, *71*, 928–940. [[CrossRef](#)] [[PubMed](#)]

38. Roedig, P.; Vartiainen, I.; Duman, R.; Panneerselvam, S.; Stübe, N.; Lorbeer, O.; Warmer, M.; Sutton, G.; Stuart, D.I.; Weckert, E.; et al. A micro-patterned silicon chip as sample holder for macromolecular crystallography experiments with minimal background scattering. *Sci. Rep.* **2015**, *5*, 10451. [[CrossRef](#)] [[PubMed](#)]
39. Dhoub, K.; Malek, C.K.; Pfleging, W.; Gauthier-Manuel, B.; Duffait, R.; Thuillier, G.; Ferrigno, R.; Jacquamet, L.; Ohana, J.; Ferrer, J.-L.; et al. Microfluidic chips for the crystallization of biomacromolecules by counter-diffusion and on-chip crystal X-ray analysis. *Lab Chip* **2009**, *9*, 1412–1421. [[CrossRef](#)] [[PubMed](#)]
40. Pinker, F.; Brun, M.; Morin, P.; Deman, A.-L.; Chateaux, J.-F.; Olieric, V.; Stirnimann, C.; Lorber, B.; Terrier, N.; Ferrigno, R.; et al. ChipX: A novel microfluidic chip for counter-diffusion crystallization of biomolecules and in situ crystal analysis at room temperature. *Cryst. Growth Des.* **2013**, *13*, 3333–3340. [[CrossRef](#)]
41. Emamzadah, S.; Petty, T.J.; De Almeida, V.; Nishimura, T.; Joly, J.; Ferrer, J.-L.; Halazonetis, T.D. Cyclic olefin homopolymer-based microfluidics for protein crystallization and in situ X-ray diffraction. *Acta Crystallogr. Sect. D Biol. Crystallogr.* **2009**, *65*, 913–920. [[CrossRef](#)] [[PubMed](#)]
42. Huang, C.-Y.; Olieric, V.; Ma, P.; Howe, N.; Vogele, L.; Liu, X.; Warshamange, R.; Weinert, T.; Panepucci, E.; Kobilka, B.; et al. In meso in situ serial X-ray crystallography of soluble and membrane proteins at cryogenic temperatures. *Acta Crystallogr. Sect. D Biol. Crystallogr.* **2016**, *72*, 93–112. [[CrossRef](#)] [[PubMed](#)]
43. Huang, C.-Y.; Olieric, V.; Ma, P.; Panepucci, E.; Diederichs, K.; Wang, M.; Caffrey, M. In meso in situ serial X-ray crystallography of soluble and membrane proteins. *Acta Crystallogr. Sect. D Biol. Crystallogr.* **2015**, *71*, 1238–1256. [[CrossRef](#)] [[PubMed](#)]
44. Axford, D.; Aller, P.; Sanchez-Weatherby, J.; Sandy, J. Applications of thin-film sandwich crystallization platforms. *Acta Crystallogr. Sect. F Struct. Biol. Commun.* **2016**, 313–319. [[CrossRef](#)] [[PubMed](#)]
45. Sui, S.; Wang, Y.; Kolewe, K.W.; Srajer, V.; Henning, R.; Schiffman, J.D.; Dimitrakopoulos, C.; Perry, S.L. Graphene-Based microfluidics for serial crystallography. *Lab Chip* **2016**, *16*, 3082–3096. [[CrossRef](#)] [[PubMed](#)]
46. Avouris, P. Graphene: Electronic and photonic properties and devices. *Nano Lett.* **2010**, *10*, 4285–4294. [[CrossRef](#)] [[PubMed](#)]
47. Avouris, P.; Dimitrakopoulos, C. Graphene: Synthesis and applications. *Mater. Today* **2012**, *15*, 86–97. [[CrossRef](#)]
48. Wirtz, C.; Berner, N.C.; Duesberg, G.S. Large-Scale diffusion barriers from CVD grown graphene. *Adv. Mater. Interfaces* **2015**, *2*, 1500082. [[CrossRef](#)]
49. Kim, H.W.; Yoon, H.W.; Yoon, S.-M.; Yoo, B.M.; Ahn, B.K.; Cho, Y.H.; Shin, H.J.; Yang, H.; Paik, U.; Kwon, S.; et al. Selective gas transport through few-layered graphene and graphene oxide membranes. *Science* **2013**, *342*, 91–95. [[CrossRef](#)] [[PubMed](#)]
50. Li, X.; Cai, W.; An, J.; Kim, S.; Nah, J.; Yang, D.; Piner, R.; Velamakanni, A.; Jung, I.; Tutuc, E.; et al. Large-Area synthesis of high-quality and uniform graphene films on copper foils. *Science* **2009**, *324*, 1312–1314. [[CrossRef](#)] [[PubMed](#)]
51. Li, X.; Zhu, Y.; Cai, W.; Borysiak, M.; Han, B.; Chen, D.; Piner, R.D.; Colombo, L.; Ruoff, R.S. Transfer of large-area graphene films for high-performance transparent conductive electrodes. *Nano Lett.* **2009**, *9*, 4359–4363. [[CrossRef](#)] [[PubMed](#)]
52. Bird, C.L.; Kuhn, A.T. Electrochemistry of the viologens. *Chem. Soc. Rev.* **1981**, *10*, 49–82. [[CrossRef](#)]
53. Aristov, N.; Habekost, A. Electrochromism of methylviologen (paraquat). *World J. Chem. Educ.* **2015**, *3*, 82–86. [[CrossRef](#)]
54. Heyrovský, M. The electroreduction of methyl viologen. *J. Chem. Soc. Chem. Commun.* **1987**, 1856–1857. [[CrossRef](#)]
55. Chayen, N.E.; Shaw Stewart, P.D.; Blow, D.M. Microbatch crystallization under oil—A new technique allowing many small-volume crystallization trials. *J. Cryst. Growth* **1992**, *122*, 176–180. [[CrossRef](#)]
56. Schneider, C.A.; Rasband, W.S.; Eliceiri, K.W. NIH image to ImageJ: 25 years of image analysis. *Nat. Methods* **2012**, *9*, 671–675. [[CrossRef](#)] [[PubMed](#)]

